

TIME-DEPENDENCE IN RELATIVISTIC COLLISIONLESS SHOCKS: THEORY OF THE VARIABLE “WISPS” IN THE CRAB NEBULA

ANATOLY SPITKOVSKY*

Kavli Institute for Particle Astrophysics and Cosmology,
Stanford University, P.O. Box 20450, MS 29, Stanford, CA 94309

JONATHAN ARONS

Astronomy Department, Physics Department and Theoretical Astrophysics Center, University of California, Berkeley, CA 94720
Accepted to Astrophysical Journal

ABSTRACT

We describe results from time-dependent numerical modeling of the collisionless reverse shock terminating the pulsar wind in the Crab Nebula. We treat the upstream relativistic wind as composed of ions and electron-positron plasma embedded in a toroidal magnetic field, flowing radially outward from the pulsar in a sector around the rotational equator. The relativistic cyclotron instability of the ion gyration orbit downstream of the leading shock in the electron-positron pairs launches outward propagating magnetosonic waves. Because of the fresh supply of ions crossing the shock, this time-dependent process achieves a limit-cycle, in which the waves are launched with periodicity on the order of the ion Larmor time. Compressions in the magnetic field and pair density associated with these waves, as well as their propagation speed, semi-quantitatively reproduce the behavior of the wisp and ring features described in recent observations obtained using the *Hubble Space Telescope* and the *Chandra X-Ray Observatory*. By selecting the parameters of the ion orbits to fit the spatial separation of the wisps, we predict the period of time variability of the wisps that is consistent with the data. When coupled with a mechanism for non-thermal acceleration of the pairs, the compressions in the magnetic field and plasma density associated with the optical wisp structure naturally account for the location of X-ray features in the Crab. We also discuss the origin of the high energy ions and their acceleration in the equatorial current sheet of the pulsar wind.

Subject headings: acceleration of particles – ISM:individual (Crab Nebula) – pulsars:general – pulsars: individual (Crab Pulsar) – shock waves

1. INTRODUCTION

The mechanisms through which compact objects excite surrounding synchrotron nebulae are one of the long-standing problems of high-energy and relativistic astrophysics. The loss of rotational energy from the central magnetized object underlies the synchrotron emission observed from pulsar wind nebulae (PWNs; e.g., Bandiera, Amato, & Woltjer 1998) and is one of the prime candidates for the energization of the jets in active galactic nuclei, radio galaxies (see Krolik 1999), and gamma ray bursts (e.g., Blandford 2002). PWNs form the nearest at hand laboratories for the investigation of the physics of such high-energy particle acceleration, and are the example where rotational energization clearly bears responsibility for the nonthermal activity.

Despite intensive study, however, the physics of how the rotational energy gets converted to the observed synchrotron emission has not been satisfactorily understood. Magnetohydrodynamic wind models (Kennel and Coroniti 1984a,b and many subsequent efforts) provide an adequate macroscopic description of the “bubbles” of synchrotron-emitting particles and fields surrounding young ($t \sim 10^3$ yr) rotation-powered pulsars, but identification and quantitative modeling of the mechanisms that convert the unseen energy flowing out from the central pulsar into the visible synchrotron emission have remained elusive.

Most attention has focused on the idea that the outflow is a supersonic and super-Alfvénic wind, perhaps with embedded large-amplitude electromagnetic waves (Rees and Gunn 1974;

Melatos and Melrose 1996). Kennel and Coroniti’s model simplified the picture by assuming the wind to be steady, with no wave structure. In that case, most models attribute the conversion of relativistic outflow energy to the nonthermal particle spectra that emit the observed synchrotron radiation in the body of the PWN to a relativistic collisionless shock wave that terminates the flow. This idea was originated by Rees and Gunn, who also observed that the shock should form at a radius where the dynamic pressure of the outflow is approximately equal to the pressure of the surrounding nebula. They also noted that in the case of the Crab Nebula, this radius approximately corresponds to the location of the moving “wisps” discovered 80 years ago (Lampland 1921) in optical observations of that PWN. This identification has motivated many studies of the wisps, as possible direct manifestations of the shock wave thought to underlie the transformation of outflow energy into the nonthermally emitting particles in the nebula.

Shortly after the discovery of the Crab pulsar, Scargle (1969) described these motions in more detail and attempted to interpret them as wave phenomena in the nebula stimulated directly by glitches in the pulsar’s rotational spin-down (Scargle & Harlan 1970; Scargle & Pacini 1971). Subsequent observations made clear that the association of wisp activity to pulsar rotational activity was a spurious consequence of undersampling the variability of the wisp motions.

The advent of the magnetohydrodynamic model has focused attention on the wisps’ structure and variability as a probe of the physics of the region where the pulsar’s outflow interacts with the nebular plasma. Substantially improved ob-

*Chandra Fellow

servations in the optical (Hester et al. 1995; Tanvir, Thomson, & Tsikarishvili 1997; Hester 1998a; Hester et al., 2002), radio (Bietenholz, Frail, & Hester 2001) and X-ray (Mori et al. 2002; Hester et al. 2002) now make it possible to test relatively refined theories of the shock's structure and particle acceleration properties.

A number of ideas have been suggested for the physics behind the observed dynamic behavior. Hester (1998a) suggested that the wisp structures reflect synchrotron cooling at constant pressure of the particles whose outflow momenta randomize at a shock in a magnetized electron-positron plasma to a power-law distribution of particles with slope in energy space flatter than E^{-2} , an idea that requires the X-ray spectrum of the plasma in the wisp region to be flatter than $\varepsilon^{-1.5}$ (X-ray flux in photons/keV-cm²-sec). However, only the particles with energy high enough to emit nebular gamma rays ($\varepsilon > 10\text{MeV}$) have synchrotron loss times short enough to create a cooling instability whose time scales are comparable to the observed variations in the optical and X-ray, and the gamma ray spectrum of the Crab (presumably arising in a compact region around the pulsar no larger than the X-ray source) has a spectral index steeper than 1.5. Chedia et al. (1997) suggest that a drift instability of a subsonically expanding plasma (no shock wave) can explain the wisp structure – how the outflow from the pulsar escapes catastrophic adiabatic losses is not addressed, however. Begelman (1999) suggests that the wisps represent the nonlinear phase of a Kelvin-Helmholtz instability between subsonic layers expanding in the rotational equator of the pulsar and flow at higher absolute latitude moving with a different velocity.

All of these ideas follow Kennel and Coroniti in assuming that the pulsar's outflow decelerates in a shock wave of unobservably small thickness, with the wisp dynamics due to phenomena in the post shock plasma (or, in the case of the Chedia et al. model, do without a shock completely). In contrast, Gallant and Arons (1994, hereafter called GA), building on earlier work on the structure and particle acceleration characteristics of relativistic shock waves in collisionless, magnetized electron-positron (Langdon, Arons, & Max 1988; Gallant et al. 1992) and electron-positron-ion (Hoshino et al., 1992) plasmas, attributed the observed wisp structure to the *internal* structure of an electron-positron-ion shock wave. The idea is motivated by the fact that the gyration of the heavy ions within the shock transfers energy to positrons and electrons through emission of ion cyclotron waves (formally, the magnetosonic mode of the magnetized electron-positron plasma). This leads to the formation of nonthermal particle spectra in rough agreement with the particle spectra required to explain the optical, X-ray, and gamma-ray emission, if the ions carry a large fraction of the pulsar's total energy loss, at least in the equatorial sector illustrated in Figure 1. The deflection of the ions' outflow by the magnetic field deposits a large amount of compressional momentum in the magnetic field, which is transverse to the flow, and into the e^\pm plasma frozen to the field. These compressions appear as brightenings in the surface brightness of the nebula. GA showed that their steady flow model gives a good account of a single high-resolution *I*-band image of the wisps (van den Bergh & Pritchett 1989). However, the wisps are known to be highly variable, on a time-scale of weeks to months. An adequate account of their behavior requires a time-dependent theory.

In this paper we present a model for time-variability of the wisp region in the Crab by extending the work of GA to include the time dependence in the flow. As was realized early

on by Hoshino et al. (1992) and Gallant et al. (1992), the coherent ion orbits invoked in the model of GA are unstable to gyrophase bunching and emission of magnetosonic waves. We find that this instability introduces a time dependence into the shock in the pair-ion plasma that causes the variable surface brightness to have substantial similarity to the observed variability of the wisps. Because of the presence of the continuous stream of fresh ions passing through the pair shock, the relativistic ion cyclotron instability provides a mechanism for sustained periodicity and wave emission dynamics that closely reproduces time-resolved observations of the wisps.

In §2 we describe the model and the underlying assumptions. In §§3 and 4, we present the results of the simulations and the dynamical predictions for the wisp region and compare them to observations. In §5, we discuss the model's successes, with emphasis on its applicability to other PWNs that have wind-nebula dynamics not very affected by radiation losses, as well as the model's limitations, pointing out further improvements needed in order to make fully quantitative comparisons with observations. We also discuss some observational tests of the ideas at their current level of development in this section. In §5.4 we describe a scenario for the origin of the high-energy ions and their acceleration in the equatorial region of the pulsar wind. Our conclusions are summarized in §6. The technical details of our hybrid numerical approach are left for the Appendix.

2. THE MODEL

Following GA, we assume that the equatorial wind of the Crab pulsar consists of relativistic electron-positron pairs and an ionic component, which is minor in number density but energetically significant. Because the ion gyration timescale is much larger than that of the pairs, we resort to a hybrid model of the termination shock in the wind. In it, the ions are treated kinetically, while the pair component is modeled as an MHD fluid. When the magnetization of the wind is small, the system is nearly charge and current neutral (see Appendix for derivation; eq. (A14-A15)). Therefore, the charge and current density in the pairs can be found by following the ion dynamics.

We assume the flow to be spherically symmetric in a 20° sector about the equatorial plane. Using the spherical coordinates (r, θ, ϕ) centered on the pulsar, and allowing for variation of all quantities with r only, the conservation laws for mass, momentum, energy, and the field evolution equations can be written as

$$\frac{\partial}{\partial t}(\rho\gamma) + \frac{1}{r^2} \frac{\partial}{\partial r}(r^2 \rho\gamma\beta_r) = 0, \quad (1)$$

$$\frac{\partial}{\partial t}(\rho h\gamma^2\beta_r) + \frac{1}{r^2} \frac{\partial}{\partial r}(r^2 \rho h\gamma^2\beta_r^2) + \frac{\partial}{\partial r}P_\perp + \frac{P_\perp - P_\parallel}{r} - \frac{1}{r} \rho h\gamma^2\beta_\theta^2 + \epsilon N_i(\beta_{i\theta} - \beta_\theta)B_\phi = 0, \quad (2)$$

$$\frac{\partial}{\partial t}(\rho h\gamma^2\beta_\theta) + \frac{1}{r^2} \frac{\partial}{\partial r}(r^2 \rho h\gamma^2\beta_r\beta_\theta) + \frac{1}{r}(\rho h\gamma^2\beta_r\beta_\theta) + \epsilon N_i(\beta_r - \beta_{ir})B_\phi = 0, \quad (3)$$

$$\frac{\partial}{\partial t}(\rho h\gamma^2 - P_\perp) + \frac{1}{r^2} \frac{\partial}{\partial r}(r^2 \rho h\gamma^2\beta_r) + \epsilon N_i(\beta_{i\theta}\beta_r - \beta_{ir}\beta_\theta)B_\phi = 0, \quad (4)$$

$$\frac{\partial}{\partial t}B_\phi + \frac{1}{r^2} \frac{\partial}{\partial r}(r^2 B_\phi\beta_r) - \frac{B_\phi\beta_r}{r} = 0 \quad (5)$$

where ρ and h are the pair density and specific enthalpy in

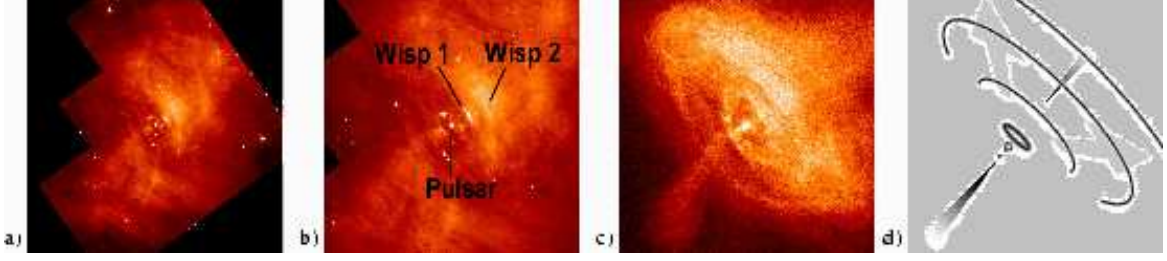


FIG. 1.— (a) HST optical image of the inner Crab Nebula (after Hester 1995), (b) Zoom in on the wisp region. (c) X-ray nebula from *Chandra* (after Weisskopf 2000; [b] and [c] are nearly to scale); (d) Illustration of the polar jet and the equatorial flow geometry of the Crab wind. *This figure is also available in color in the electronic edition of the Astrophysical Journal*

the proper frame, $\gamma\beta$ is the 4-velocity of the pairs, $N_i = n_i\gamma_i$ is the observer's frame density of the ions, and B_ϕ is the toroidal component of magnetic field, which is the only magnetic field component that we consider in the equatorial plane. P_\perp and P_\parallel are the components of the pair plasma's pressure tensor perpendicular and parallel to B . The field is normalized by the upstream value B_1 , and expression (6) defines ϵ . Since we are interested in the dynamics on the ion gyration scale, we normalize time by ω_{ci1}^{-1} and radius by r_{Li1} , where $\omega_{ci1} = ZeB_1/\gamma_{i1}m_i c$ and $r_{Li1} = c/\omega_{ci1}$ are the upstream values of the relativistic cyclotron frequency and ion Larmor radius, respectively, and Ze is the ion charge. We normalize the enthalpy and pressure by the upstream kinetic energy of the pairs $m_\pm c^2 N_{1\pm} \gamma_1$, where $N_{1\pm} = \gamma_1 n_{1\pm}$ is the pair number density in the observer's frame. After traversing the shock, the pairs are confined to the plane perpendicular to the toroidal magnetic field until pitch-angle scattering isotropizes the pair distribution function. We allow for the anisotropic pressure in the directions perpendicular and parallel to the magnetic field, $P_\perp \neq P_\parallel$. These components of the pressure tensor are related through the adiabatic index Γ such that $P_\perp = (\Gamma - 1)\epsilon$, where $\epsilon = 2P_\perp + P_\parallel$ is the internal thermal energy of the pairs. This results in $\Gamma = (3 + P_\parallel/P_\perp)/(2 + P_\parallel/P_\perp)$ with Γ decreasing from $3/2$ to $4/3$ as pressure isotropizes. In our model we simulate the effect of pitch-angle scattering in the pairs by gradually decreasing Γ with distance from the pair shock over a distance of 0.05 pc (for further discussion of theory and simulation of pitch-angle scattering in magnetized electron-positron-ion plasmas see Yang et al. 1993; Yang, Arons, & Langdon 1994). The relative fractions of the preshock wind energy carried by the ions, the pairs and the Poynting flux are parameterized using

$$\begin{aligned} \sigma_\pm &\equiv \frac{B_1^2/4\pi}{N_{1\pm}m_\pm\gamma_1c^2}, & \sigma_i &\equiv \frac{B_1^2/4\pi}{N_{1i}m_i\gamma_{i1}c^2}, \\ \epsilon &\equiv \frac{\sigma_\pm}{\sigma_i} = \frac{N_{1i}m_i\gamma_{i1}c^2}{N_{1\pm}m_\pm\gamma_1c^2}, \end{aligned} \quad (6)$$

where σ_\pm and σ_i are the initial magnetization of the pairs and ions, respectively. Global models of the nebula (e.g., Kennel and Coroniti 1984a) constrain the total magnetization $\sigma_{\text{tot}} \equiv (1/\sigma_\pm + 1/\sigma_i)^{-1}$ to be small, ~ 0.003 . Because of the small initial magnetization of the wind and our attention to the region near the termination shock, we neglect the terms proportional to σ that otherwise would enter into (1-4) (see Appendix for the full equations).

Equations (1-4) describe the system of evolution equations that we solve numerically to find the time-variability of the collisionless shock structure. We use the particle-in-cell (PIC)

method (Birdsall and Langdon 1991) for advancing ions and calculating their current and charge density, while the pairs are evolved by finite-differencing the MHD equations on a one-dimensional mesh. Particular attention is paid to the boundary conditions, with an outflow nonreflecting condition (Thompson 1987) implemented on the downstream boundary.

The inner boundary condition for the pair plasma and magnetic field comes from the jump conditions for an infinitesimally thin shock wave in the pair plasma, as in Kennel and Coroniti (1984a). The shock is located inside the domain and the flow is extrapolated upstream to the injection boundary at $0.1 r_{Li}$. The ions enter as a cold stream at the inner boundary, all with identical energy $\gamma_1 m_i c^2$, where γ_1 is the Lorentz factor of the upstream wind – we assume that the upstream ions and pairs flow with the same 4-velocity. The jump conditions at the pair shock are such that the magnetic field increases by a factor of $1/(\Gamma - 1)$ over its value in the upstream wind, and the velocity of pair flow decreases by the same factor, while the tangential electric field is continuous through the shock. The ion stream, therefore, starts to gyrate as well as $\mathbf{E} \times \mathbf{B}$ drift in the magnetized pairs as shown in Fig. 2a. The turning points in the ion orbits are regions of strong vertical current that, through the $\mathbf{j} \times \mathbf{B}$ force, provide a compression on the pairs. This compression results in locally higher density of the pairs at each ion turning point, and compression of the frozen-in magnetic fields. This field, in turn, affects the motion of the ions, and hence the initial configuration is bound to change. Although it is possible to load the ions and the fields in a self-consistent static configuration, we find that the result of the dynamical simulation is independent of the initial load method. We describe the dynamical simulations in the next section.

3. SHOCK DYNAMICS

The coherent ion loops generated during ion transit through the pair shock are an excellent environment for the growth of a relativistic ion cyclotron instability. This is a variant of the classic instability of a “ring in momentum space” and proceeds via gyrophase bunching and subsequent phase mixing. The crucial distinction in the shock case from the development of the instability in a uniform plasma is that there is a preferred direction of the flow, so that the time development of the instability is spread out in space as the ions undergo $\mathbf{E} \times \mathbf{B}$ drift into the shocked pairs. The typical growth rate is on the order of the ion Larmor time (Hoshino & Arons 1991) in the postshock field, and within the first ion loop gyro bunching develops characteristic “knots,” shown in Figure 2b. Beyond several orbits in the postshock field the instability has taken its course, and the downstream ion orbits become chaotic, with

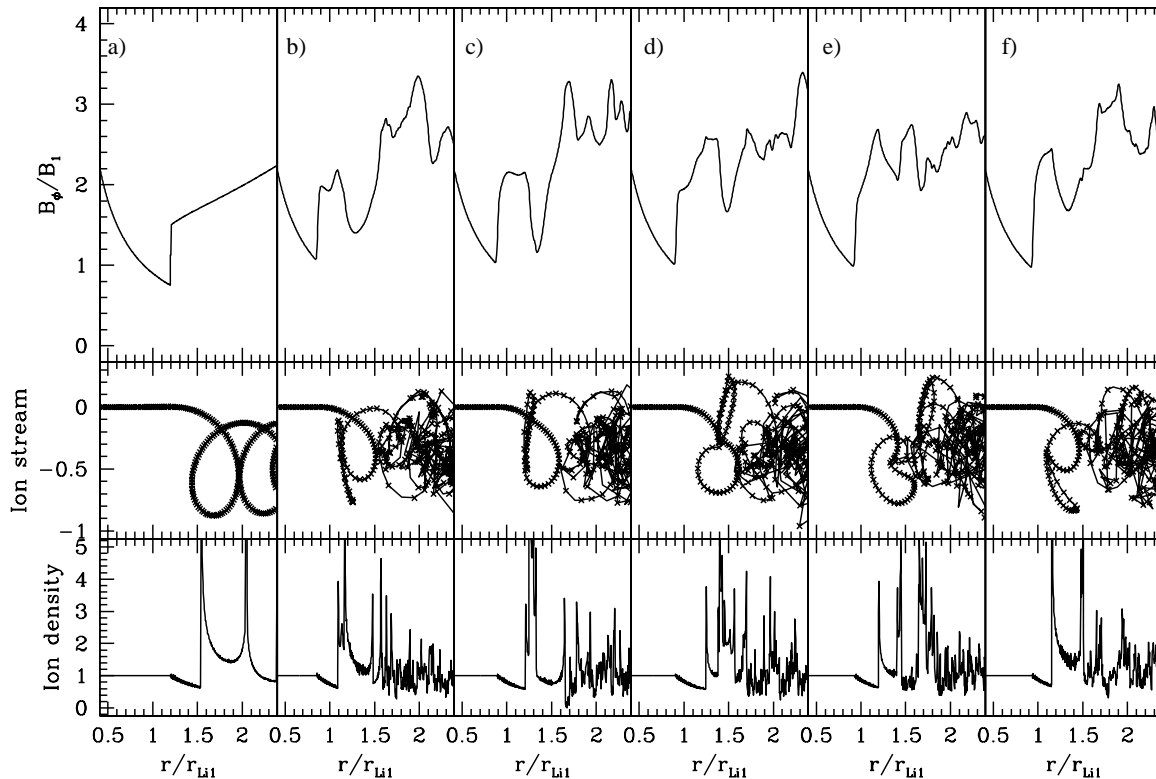


FIG. 2.— Phases of the limit cycle. *Top*: Magnetic field, in units of preshock value B_1 , vs. distance. *Middle*: Ions’ momenta through the shock, with length units of preshock ion Larmor radii. *Bottom*: Ion density in the radial direction, with density normalized to the preshock ion density. The unit of length is the ion Larmor radius based on upstream parameters, r_{Li1} . The columns are as follows: (a) Initial state of the $\Gamma = 3/2$ shock with Γ decreasing to $4/3$ by $r = 1.5r_{Li1}$. The cold ion stream is loaded through the pair shock without affecting the field structure. (b-f) Developed limit cycle. A gyroknott advects around the ion ring and triggers the next cycle upon leaving the region. This figure is also available as an mpeg animation in the electronic edition of the *Astrophysical Journal*.

the ion distribution eventually relaxing to a quasi-Maxwellian form. However, in the case of a shock in a relativistic flow and in our simulation, the cold ions are continuously flowing through the shock, thus constantly refreshing the instability’s flagging spirits.

The interplay between the low entropy input of ions and the randomizing cyclotron instability creates interesting dynamical consequences for the region of the first ion gyration loop. In this region we observe the development of a limit cycle, in which the first ion loop develops gyroknotted ion knots that are advected downstream with the overall $\mathbf{E} \times \mathbf{B}$ flow. As one knot is leaving this region, it creates an enhanced magnetic field that triggers the development of a new “gyroknott,” which goes around the ion ring and the process repeats. The snapshots of the phases in this limit cycle are shown in Fig. 2b-f.

In these frames we display the magnetic field, the ion stream flowing through the shock, and the corresponding ion density. The postshock magnetic field shows the characteristic “double-horn” structure due to compressions in the pair density at the turning points of the zeroth-order ion drift orbit. The development of the cyclotron instability in the first ion loop introduces additional compression in the field because the gyroknotted ions exert additional $\mathbf{j} \times \mathbf{B}$ stress on the pairs. As the gyroknott is advected around the ion loop, the associated compression in the pairs launches magnetosonic waves. The area of the first ion ring can be thought of as the near zone of a radiating region, while the flow further downstream represents the wave zone. As the wave propa-

gates between the turning points in the first ion loop, it imprints a moving component in the double-horn structure of the magnetic field. When this compression in the field reaches the second ion turning point, it triggers gyroknotted ions. The period of the cycle is found from simulations to be $\sim 0.5T_{Li}$, where $T_{Li} = 2\pi/\omega_{Li}$ is the Larmor time for the ions in the *postshock* field. The cycle period can be understood as roughly the time in the laboratory frame that it takes for the ion to go around one loop in the $\mathbf{E} \times \mathbf{B}$ drift orbit, or $[(1 - \beta_d)/(1 + \beta_d)]^{1/2}T_{Li}$, where $\beta_{dc} = (\Gamma - 1)c$ is the initial drift speed in the downstream region.

4. APPLICATION TO THE WISPS’ DYNAMICS

As did GA, we interpret the wisp region in the Crab as a collisionless shock in the pair plus ion plasma. Although the ions are not directly observed, the compressions in the pair density and magnetic field associated with the turning points in the ion orbit should result in regions of increased synchrotron brightness. GA associated the first two ion turning points with wisp 1 and wisp 2 (see Fig. 1b). Our time-dependent analysis augments this interpretation with additional features. We find that the back-and-forth motion of the gyro-knott in the region of the first ion ring acts as a periodic source of magnetosonic waves that make the shock structure very dynamic. The magnetosonic waves that propagate back toward the pair shock are reflected from it and compress the magnetic field near the shock, brightening wisp 1. As the waves propagate from wisp 1 to wisp 2, they appear as a moving bright feature, a “moving wisp,” that brightens the region of wisp 2 when it crosses it.

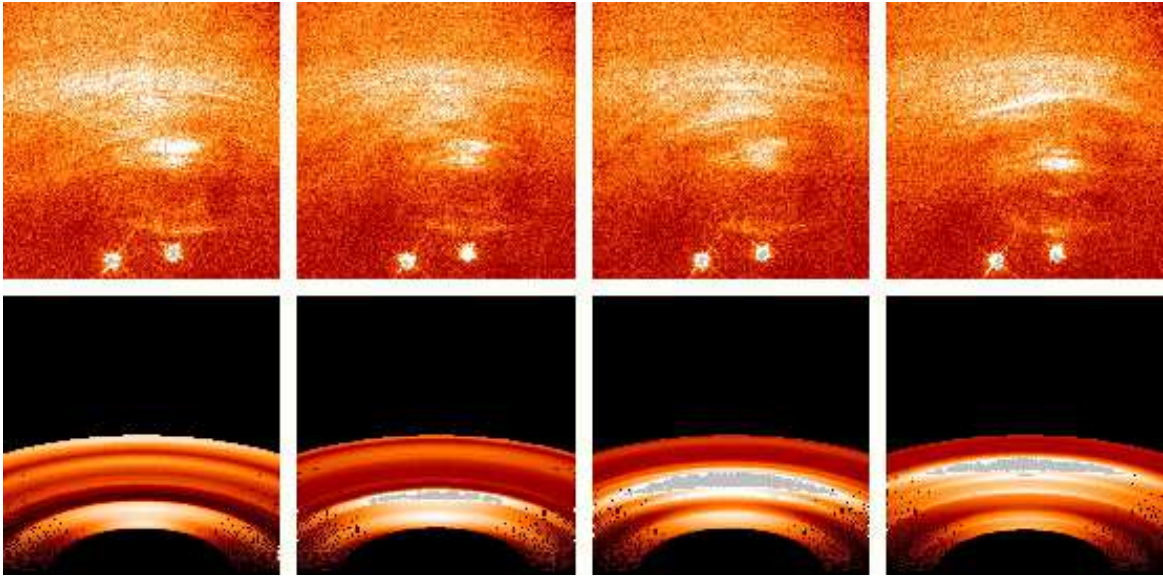


FIG. 3.— *Top*: *HST* snapshots of the wisp region in the Crab. Separation between the first and the last pair of frames is 3 weeks; middle frames are separated by a week. The observation interval is from 1995 December 29 to 1996 February 22. Data were extracted from the *HST* archive (observations by J. Hester). *Bottom*: Simulated surface brightness of the wisp region. The moving wisp is being emitted from the first wisp and propagates toward the second wisp. Fine filamentary structure is created in the second wisp region. This figure is also available in color and as mpeg animation in the electronic edition of the *Astrophysical Journal*.

The sequence of propagation and brightening of the features is choreographed by the underlying limit cycle of the instability in the first ion loop. The overall timescale of the limit cycle can be obtained by choosing the preshock ion Larmor radius r_{Li1} such as to fit the observed separation of the wisps 1 and 2 with the separation of compressions in the model. The limit cycle then occurs with the period $T_{cycle} \approx \frac{1}{2} T_{Li} = \pi(\Gamma - 1)r_{Li1}/c$. Here we used the magnetic field jump conditions to express the postshock Larmor time in terms of preshock quantities. For typical values $\Gamma = 3/2$, $r_{Li1} = 0.1$ pc we get $T_{cycle} \approx 6$ months.

We have taken our one-dimensional profiles of the magnetic fields, pair density and pair velocity to construct the sequence of simulated surface brightness maps of the wisp region in the optical band. We assume that in the proper frame the pair flow emits synchrotron radiation as a relativistic Maxwellian. This is essentially a monoenergetic emission and represents the surface brightness distribution in space for any relatively narrow bandpass from pairs whose Larmor radii are small compared to the ion Larmor radius (photon energies below 10 MeV). The radiation from the flow moving along the equatorial plane, tilted by $\sim 65^\circ$ from the plane of the sky, is further Doppler boosted and beamed on the way to the observer. The resulting maps, shown in Fig. 3, are a qualitative picture of the way the features in the wisp region should appear. The Doppler beaming makes the faster flow near the shock appear to have smaller angular extent than slower flow in the region of wisp 2. For comparison, we also reproduce snapshots from 1995-96 *Hubble Space Telescope* (*HST*) observations of the inner nebula during a moving feature emission episode in the same figure (Hester et al. 1998b). Observations from the 2000-2001 *HST* campaign (Hester et al. 2002) show very similar dynamics of the features. In principle, the simulated brightness profile can be constructed for the X-ray band as well and will look very similar to the optical image. This procedure will, however, overpredict the amount of beaming and make the inner *Chandra* ring appear as two disjoint arcs, contrary to observations. We comment further on this discrepancy

in §5.2.

Using the simulated surface brightness maps we can describe the time dependent behavior of the wisp region throughout the cycle of emission according to our model:

- 1) The emission of a major moving wisp is preceded by a brightening and thickening of wisp 1. This may also appear as a forward motion of wisp 1. After the emission, it dims and retracts to the original position. In general, the oscillating pressure of magnetosonic waves in the wisp region causes oscillation in the position of the shock in the pairs. This can make wisp 1 appear as oscillating with the cycles of emission of the moving wisps. The amplitude of this oscillation is relatively small ($< 10\%$ of the distance between wisp 1 and the pulsar).
- 2) The compression associated with the moving wisp increases in brightness while propagating toward wisp 2. Because of this, the moving wisp appears to turn on some distance away from wisp 1 ($< 20\%$ of the distance between wisp 1 and wisp 2). The moving wisp appears as a fairly sharp feature.
- 3) The region of wisp 2 is located at the interface of the first and second ion loops. By the second gyration loop the ion cyclotron instability is well into the nonlinear stage, and the ion orbits are scrambled and chaotic. This ion background provides a large amount of short-wavelength features that comove with the flow as the ions drift downstream. In fact, observations by Hester et al. (1995) indicate that wisp 2 has a fine fibrous structure. We attribute the creation of such filaments to the chaotic ion background. Although the fine filaments should appear moving away from the shock roughly with the flow velocity, we expect that new filaments can appear in this region without having a precursor traveling all the way from the shock.

- 4) When the moving wisp propagates toward wisp 2, it brightens up wisp 2 and its surroundings. The moving wisp is a compression in the field and pair density that propagates as a fast magnetosonic wave. This wave was emitted from the first postshock ion gyration loop and travels at the fast magnetosonic speed on top of the background pair flow. In the case of low magnetization the wave speed is given by $c(\beta_{\text{flow}} + \sqrt{\Gamma - 1}) / (1 + \beta_{\text{flow}} \sqrt{\Gamma - 1})$. Assuming that the pairs have isotropized in the region of the second wisp, so that $\Gamma = 4/3$, we get $v_{\text{wisp}} \approx 0.6c$ as would be seen in the equatorial plane of the Crab. When the moving wisp traverses wisp 2, it overtakes slower moving fibrous filaments, and causes more filaments to be created in its wake, as it scatters on the random ion background.
- 5) The propagation of the fast-moving wisp from the first to the second wisp takes about half the cycle of the wisp emission (~ 90 days). For the second half of the cycle no major brightening occurs, until the first wisp starts to brighten again, indicating the beginning of the next cycle. This behavior paradoxically results in the wisp structure appearing both stationary and moving at the same time. On average there are always two bright regions corresponding to the first and second wisps, with the second wisp being more diffuse. These regions correspond to compressions due to the turning points in the first ion loop, which are more or less fixed in space, but can oscillate in brightness. At the same time, the instability in the ion gyration produces intermittent wisps that move between the first and second wisp at the magnetosonic speed and change the brightness of the main wisps as they compress the plasma and the field. Yet, the first and second wisps do not move as a wave themselves.

The model has several parameters that we can vary to study the shock dynamics in qualitatively different regimes. The main parameters are the ratio f of the preshock ion Larmor radius to the radius r_s of the shock in the pairs, $f \equiv r_{Li1}/r_s$, and the relative fraction ϵ of the energy density carried by the ions and the pairs (eq. [6]). The parameter f controls the degree to which spherical geometry affects the shock dynamics. For small values of f , the background flow is essentially plane-parallel on the ion gyration scale, and the ions do not experience the gradient in the background magnetic field. For the Crab parameters, $f \sim 1$, so the effects of spherical geometry are important. Increasing f decreases the separation of the turning points in the ion orbit and changes the relative strength of plasma compressions corresponding to the turning points, as illustrated in Figure 7 of GA. The parameter ϵ controls the amount of influence the ions have on the pair fluid. For small ϵ the underlying pair shock structure is hardly perturbed. This makes the instability grow at a slower rate, and the first several ion loops may appear steady. The gyro-knots, characteristic of the instability, then appear only several Larmor radii downstream. In the limit $\epsilon \rightarrow 0$ there is, of course, no instability, and the ions and the pairs are decoupled. For finite ϵ , once the instability proceeds, the period of the limit cycle is not sensitive to ϵ , and is approximately half of the local Larmor time of the ions. We fix the value of $f \approx 1.2$ to match the separation of the wisps with the compressions at the turning points in the ion orbits. We then vary ϵ to achieve the conditions where both the instability grows sufficiently by the

time the ions cross the first ion loop, and the compressions in the magnetic field and the density result in the intensity variations consistent with observed variation in the nebula. For perturbations $\delta B/B \sim 1$ we need $\epsilon \sim 1$. For the pair injection rate of $\dot{N}_{\pm} \approx 10^{38} \text{ s}^{-1}$ needed to explain the X-ray source in the Crab, we then find that the ion injection rate should be $\dot{N}_i = \epsilon m_{\pm} / m_i \dot{N}_{\pm} \approx 10^{34} \text{ s}^{-1}$ if we assume that the ions are helium (the model favors ions with a Z/A ratio of ~ 2 , which could be either He or Fe). These ions travel with the same Lorentz factor (10^6) as the equatorial pair wind.

5. DISCUSSION

5.1. Model Successes

The theory outlined here has a number of virtues in its description of the physics of the termination of the Crab pulsar's equatorial wind. The timescale and length scales of the observed optical and X-ray variations can be semi-quantitatively reproduced, for entirely reasonable values of the ion energy. Granted the approximate validity of the underlying Kennel and Coroniti (1984a) flow model, for ions that accelerate through a fraction $\sim 0.1 - 0.2$ of the available open field potential $\Phi \approx 4 \times 10^{16} \text{ V}$ to energies $\sim 0.15Ze\Phi \approx 6 \times 10^{15} \text{ eV}$, the ion Larmor radius, which sets the wavelength scale of the moving features, is $r_{Li} \sim 10^{18} B_{s16}^{-1} (r_s/r)$ cm. Here $r_s \leq 1.5 \times 10^{17} \text{ cm}$ is the radius of the shock in the pairs, located at or interior to the *Chandra* X-ray ring and $B_s = \sigma^{1/2} B_{\text{nebula}} \approx 16 B_{s16} \mu\text{G}$. The ion energy is obtained by asking the model to replicate the spacing of the moving features in the optical and X-ray images. The ions are deflected and become magnetically well coupled to the pair plasma in the increasing magnetic field at $r > r_{\text{turning}} = [r_{Li}(r_s)r_s]^{1/2} \approx 4 \times 10^{17} (\gamma_{i6.5}/B_{s16})^{1/2} \text{ cm}$. This is the radius at which the compressional limit cycle formed by the first ion loop stands as a quasi-stationary feature in the pair flow. Given the close resemblance between this feature of the model and the behavior of the *Chandra* X-ray ring, it is tempting and natural to identify the X-ray ring with the first ion loop's turning points. If so, the quasi-stationarity of this feature then has a natural explanation, as being the consequence of the ion cyclotron instability within the shock structure, without having to invoke extra physics and an otherwise unexplained external stimulus to account for the time scale of the ring's repetitive variations. The non-axisymmetric knotted structure of the ring might be explainable as the consequence of instabilities of the mirror type, driven by the reflected ions' pitch angle anisotropy with respect to the toroidal magnetic field – a topic well beyond the scope of the current investigation, however.

The model also gives a natural interpretation of the moving features in both optical and X-ray, as compressional waves in the pair plasma emitted by the time variable ion currents in the first loop limit cycle. These modes are a mixture of magnetosonic waves moving with respect to the plasma flow and entropy and slow modes frozen into the flow. This behavior supports the identification of the *Chandra* ring as the location of the ion limit cycle structure, since that ring's appearance suggests it to be the wave emission zone.

The theory is adiabatic with respect to radiation losses from the pairs; that is, the formation of the ring and the moving wisps does not depend on the synchrotron loss times of the pairs being comparable to or shorter than the local flow time in the vicinity of the ring. Since ringlike and wisp features have been discovered near pulsars in other PWNs at radii where dynamic pressure balance arguments suggest formation

of wind termination shocks, yet all occur in systems whose synchrotron cooling times even for X-ray-emitting particles are larger than the local flow times, the theory developed here appears to have general applicability, in contrast to models that depend on the unusually strong magnetic fields and short synchrotron cooling times prevalent in the Crab Nebula (e.g., Hester 1998a; Hester et al. 2002). Gaensler et al. (2002) give an example of our theory's use, in the interpretation of the X-ray features observed close to PSR 1509-58.

This model has a substantial theoretical virtue: the required ion flow has the magnitude expected if it is the electric return current (Goldreich-Julian current) that should exist in the rotational equator of the pulsar's wind (Michel 1974; Contopoulos et al. 1999), which prevents the star from charging up when non-vacuum torques are a significant contributor to spindown. This conclusion is the same as was reached by GA from a time-independent flow model, now seen as a robust consequence of the fully time-dependent theory.

5.2. Model Limitations and Failures

There is a substantial ($\sim 20\%$) discrepancy between the velocities of the moving magnetosonic wave features computed in the model (0.6c) and the speeds of the observed features [$\sim 0.5c$, in the geometry adopted by Hester et al. (2002), itself a velocity large compared to what one would expect, $(c/3)(R_{shock}/r)^2$, for features frozen into a simple Kennel & Coroniti 1984a flow]. This discrepancy may be related to the geometrical simplifications of the model, discussed further below, or it may be an intrinsic difficulty.

The model's one-dimensionality is a serious limitation. We assumed the flow to be strictly radial, within a spherical sector around the rotational equator. Within that sector, we assumed the magnetic field to be strictly toroidal and have a single sense of winding with respect to the rotation axis of the pulsar, independent of rotational latitude. Going along with this one-dimensionalization, we assumed the flow of pairs and ions to be completely charge neutral and to be current neutral in the radial direction. Yet we concluded that the ion flux corresponds in magnitude to an electric current flowing out in the equatorial plane with strength sufficient to qualitatively and quantitatively alter the magnetic field.

A more realistic model would take this result seriously and treat the ion flux as a net electric current in the radial direction (balanced in a quasi-steady state by a polar electron current feeding the polar jets). Such a current in the upstream wind separates two hemispheres of toroidal (and very weak radial) magnetic field that are oppositely directed in the two hemispheres. In such a field, high-energy ions in the equatorial current flow, upon crossing the shock in the pairs, are not fully reflected by the compressed magnetic field in the heated pair plasma. They are deflected from their initial radial orbits, but transfer a smaller fraction of their outward momentum into compressions of the pair plasma. Thus, the model described here somewhat overestimates the compression of the magnetic field in the region where the limit cycle appears, probably by a factor on the order of 2. Generating synthetic surface brightness maps, as a function of assumed ion and pair energy and number fluxes, that are quantitatively reliable requires taking this more realistic geometry and ion dynamics into account.

Several comments are in order regarding the speed of propagation of the wisps. Quasi-periodic temporal drive due to the ion instability leads us to interpret the moving features in the Crab as the fast MHD waves. This, however, leads not

only to overestimation of the speed of the features as outlined above, but also to an uncomfortable prediction that the wisps should reach an asymptotic velocity as they propagate downstream. As the background flow decelerates, the speed of the disturbance decreases to the sound speed $\sqrt{\Gamma-1}c = 0.58c$ for $\Gamma = 4/3$. Fast waves are not the only type of perturbations generated by the instability, however. Ion motion also excites entropy, Alfvén and slow waves. All of these perturbations have zero phase velocity for the toroidal background magnetic field; therefore, they are advected with the flow. The entropy wave does not have any perturbation in the magnetic field and therefore will not appear as bright as the modes that perturb both the density and the magnetic field. The Alfvén mode is peculiar because it is the only disturbance that has the transverse velocity perturbations. It can be advected with the ion flow that generates the perturbation in the pairs' latitudinal velocity.

As the fast wave from the emission region crosses wisp 2 and encounters the chaotic ion background beyond the first ion $E \times B$ loop, there will be some compressions in the pairs and the field that move with the average $E \times B$ velocity of the ions (which is the same as the pair flow velocity). These compressions are not free-propagating, but driven by $j \times B$ forces from ion streams. They are similar to the double-horn soliton structure generated by ion loops (Alsop & Arons 1988), but they are moving as the ion loops are advected with the unstable ion stream. Therefore, at larger distances it is reasonable to expect wisplets that appear to move with the background flow. However, such features would be relatively short lived (approximately a month) and would appear to come seemingly from nowhere. Therefore, beyond wisp 2 we expect to see two populations of wisps – ones moving with the background decelerating flow (slow magnetosonic and Alfvén waves), and fast magnetosonic perturbations that can be traced back to the shock in the pairs at wisp 1. The intensity of the fast compressions will get diminished with distance, and they will naturally blend into slower background flow. A clear observational tracking of a single feature through the whole flow (with snapshots separated by no more than 2 weeks) would be very beneficial to settling the issue of the speed of the flow and the nature of the speed of the features.

The front-to-back asymmetry of the optical wisps' brightness has an obvious interpretation in the Doppler boosting enforced by the underlying flow, which preserves on average the Kennel and Coroniti radial profile $v_r = (\Gamma - 1)c(r/R_s)^2$. However, the inner *Chandra* ring does not show such obvious asymmetry, even though it appears to be spatially collocated with wisp 1. If this apparent symmetry is real, our identification of the first ion turning point with the *Chandra* ring obviously conflicts with our interpretation of the optical wisps. We believe that this discrepancy is another manifestation of the one-dimensional model's limitations. If the *Chandra* ring forms in the equatorial current layer, which is embedded in a higher latitude ($|\lambda| > 10^\circ$) flow (Begelman 1999), perhaps having higher σ (Arons 2004), the flow right in the equator might have lower velocity than the higher latitude component, with the optical wisps being features stimulated in the higher latitude flow by the large Larmor radius ions. Such a multi-dimensional environment, which is implied by the ions being a net electric current, then might account for Doppler boosting of the optical wisps along with smaller or negligible Doppler boosting of the X-ray features. Testing dynamical

viability of such a scheme awaits the development of a two-dimensional, axisymmetric model, whose MHD aspects are likely to be similar to the nebular model recently proposed by Komissarov and Lyubarsky (2003).

5.3. Nonthermal Particle Acceleration and Radiation

Although our dynamical model and synthetic images assume a thermal (essentially, a monoenergetic) pair distribution in the radiating plasma, they can be extended to the regime where the distribution is nonthermal, as is the case for the X-ray and optically emitting particles. The compressions in the field and plasma density associated with the shock structure should cause higher synchrotron emission for all electrons and positrons with Larmor radii smaller than the characteristic wisp separation, or for $\gamma_{\pm} < 10^{10}$, $E_{\pm} < 5 \times 10^{15}$ eV, emitting at $160 \text{ keV} < \varepsilon_{\text{max}} < 50\text{--}100 \text{ MeV}$ in the magnetic field whose strength increases from $\sim \sqrt{\sigma} B_{\text{nebula}} \approx 16 \mu\text{G}$ at the leading edge of the shock structure to $\sim 300 \mu\text{G}$ at and beyond the outer reaches of the X-ray torus (Kennel and Coroniti 1984a; de Jager and Harding 1992). Thus, the wave motions seen in the *Chandra* band should display behavior similar to the optical wisps; that is, the features emitted from the X-ray inner ring discovered by Weisskopf et al. (2000) display similar variability as the optical moving wisps, and all propagate toward and through the X-ray torus. The observations do show such resemblances, at the qualitative level.

We have identified the *Chandra* X-ray ring as the site of the limit cycle in the unstable, reflected ion stream, not as the leading edge reverse shock in the pairs. The main reason to do this is the morphological similarities between the observed ring and our synthesized image. Whether the actual pair shock is located at the *Chandra* ring as concluded by Hester et al. (2002) or interior to it depends on the shock acceleration mechanism for the pairs. Below we consider the consequences of several shock acceleration schemes.

The pair shock heats the pair plasma to characteristic particle energies $\sim \gamma_{\text{wind}} m_{\pm} c^2 \approx 10^{12} \gamma_{w6.5}$ eV, where $\gamma_{w6.5} = \gamma_{\text{wind}}/10^{6.5}$. The downstream magnetic field at and immediately behind the pair shock is weak. For $\sigma \approx 3 \times 10^{-3}$, $B \approx 16 B_{s16}(r/R_{s\pm}) \mu\text{G}$. Pairs compressed and heated by the pair shock radiate in the optical and infrared, with characteristic frequency $\nu_c = 6 \times 10^{14} \gamma_{6.5}^2(r/R_{s\pm})$ Hz. However, the synchrotron radiation time of newly shocked pairs at and just behind the pair shock is long, $T_{s\pm} \approx (3800/B_{s16}^2 \gamma_{6.5})(R_{s\pm}/r)^2$ yr, far larger than the local flow time $T_{\text{flow}} = r/v(r) = 0.5(R_{s\pm}/10^{17.2} \text{ cm})(r/R_{s\pm})^3$ yr. Thus simple shock heating of the pairs implies that optical emission does not start until $r > 10^{18}$ cm from the pulsar, which is larger than the radius of optical emission onset.

Gallant et al. (1992) demonstrated that the pair shock can indeed thermalize the upstream flow. The pair shock may, of course, also be a nonthermal particle accelerator, as has been assumed in all MHD models for the excitation of the Crab, starting with Rees and Gunn (1974). Diffusive Fermi acceleration (DFA) in transverse relativistic shocks is often invoked as the mechanism for such acceleration (see Gallant 2002 for a review). Since the energy gains per encounter of a particle with the shock are $\Delta E \sim E$, this process might turn the pair shock into a nonthermal X-ray emitter, if the cross field diffusion time is short in the downstream medium, comparable to the cyclotron time (“Bohm diffusion”) – such diffusion must occur, if the requisite multiple encounters are to exist. Diffusion speeds exceeding the downstream flow speed ($\sim c/3$) require quite strong downstream turbulence, however (Bednarz

and Ostrowski 1996), probably at levels higher than observed in the two-dimensional pair shock simulations of Gallant et al. (1992). In the absence of three-dimensional simulations that allow evaluation of the turbulence level and that also allow for cross field diffusion, DFA at the pair shock is not excluded as the means of creating nonthermal emission, although the constraints on the required diffusion rates clearly are rather demanding.

Progressive acceleration with increasing radius, due to the resonant cyclotron absorption by the pairs of the high harmonic ion cyclotron waves emitted by the ions (Hoshino et al. 1992; E. Amato & J. Arons, in preparation), is an alternate to the commonly assumed DFA that has a natural setting in the context of the ion-doped relativistic shock whose spatial structure has been modeled here. The acceleration time is approximately the ion cyclotron time, which leads to energy gains such that X-ray emission from the *Chandra* ring requires placing the now unobserved pair shock at a radius between 2 and 3 times smaller than the radius of the X-ray ring. A full discussion of this distributed acceleration model will be given elsewhere.

5.4. The Acceleration of the High Energy Ions in the Wind

So far we have not addressed the issue of how the ions are energized to the inferred values of $\gamma \sim 10^6$. One possibility is that the high energy of the ions and the high 4-velocity of the pulsar wind are due to the gradual “surf-riding” acceleration in the inner wind of the pulsar. If the wind begins near the light cylinder with $\sigma_{L0} \equiv \gamma_L \sigma(R_L) \gg 1$, where $\gamma_L \equiv \gamma(R_L)$ is the Lorentz factor of a particle injected into the wind at $r = R_L$, then particles riding on the field lines of the wind move on almost radial paths and increase their energies linearly with radius (Buckley 1977). This acceleration continues until the almost force-free, multidimensional flow in the inner region ends at the radius R_{ff} , which is not greater than $\sigma_{L0}^{1/3} R_L$, where $\sigma(r)$ drops to $\sigma_{L0}^{2/3}$ and $\gamma_{\text{wind}} \approx \sigma_{L0}^{1/3}$ (Beskin, Kuznetsova, & Rafikov 1998; J. Arons 2004, in preparation). Here R_{ff} is the radius where the flow speed first reaches the velocity of the fast magnetosonic wave; beyond this radius, the magnetic stress no longer can overcome the longitudinal inertia $\rho \gamma_{\text{wind}}^3$ of the plasma, where ρ is the rest mass density. The acceleration in the inner region has its origin in the particles being stuck to the field lines, with the balance of electromagnetic forces causing the field lines to move with an $E \times B$ velocity that is slightly below c , but increasing toward c with distance. This effect results in γmc^2 increasing linearly with radius for all particles in the wind, when $r < R_{ff}$. For $r > R_{ff}$, γ_{wind} stays approximately constant in laminar, ideal MHD relativistic flow. This conclusion has been formally demonstrated only when the poloidal field is monopolar, but is likely to be a robust conclusion in practical terms from all relevant magnetic geometries (Begelman and Li 1994; J. Arons 2004, in preparation).¹

¹ Early one-dimensional MHD models (Michel 1969; Goldreich & Julian 1970) found $\gamma \rightarrow \sigma_{L0}^{1/3}$ as $r \rightarrow \infty$, a result that is an artifact of their one-dimensional (in effect, cylindrical) flow assumptions. The fact that $R_{ff} < \infty$ in the multidimensional model of Beskin et al. (1998) results from their incorporating the transverse (to the radial flow direction) electromagnetic stresses, while their result that $R_{ff} = \sigma_{L0}^{1/3} R_L \gg R_L$ is an artifact of using a strict monopole for the poloidal magnetic field. More physical models that have modest departures of the poloidal field from the monopole have R_{ff} at most a few times R_L . Contopoulos and Kazanas (2002) are incorrect in their claim that the force free region extends to $\sim \sigma_{L0} R_L$ with $\gamma \rightarrow \sigma_{L0}$ – the accelera-

Such a linear accelerator in the inner wind, an idea recently resurrected by Contopoulos and Kazanas (2002), reaches finite-inertia saturation too soon to provide sufficient acceleration to the wind and the ions in the Crab. Our results for the particle content of the wind's equatorial sector with latitude range $|\lambda| < 10^\circ$ suggest a Goldreich-Julian flux of heavy ions $\dot{N}_i = \dot{N}_{GJ}/Z = 2\Omega^2 \mu / Zec \approx 2 \times 10^{34}/Z \text{ s}^{-1}$, and a flux of electron-positron pairs $\dot{N}_+ + \dot{N}_- = 2\kappa_\pm \dot{N}_{GJ} \approx 10^4 \dot{N}_i \sim 10^{38.3} \text{ s}^{-1}$ (Harding & Muslimov 1998; Hibschan & Arons 2001; Muslimov & Harding 2003). Then

$$\sigma_{L0} \equiv \frac{B_L^2}{4\pi[m_i n_i(R_L) + 2m_\pm n_\pm(R_L)]c^2} = \frac{1}{2} \frac{Ze\Phi}{m_i c^2} \frac{m_i}{m_{eff}}, \quad (7)$$

$$m_{eff} \equiv Am_p + 2\kappa_\pm Zm_\pm. \quad (8)$$

For Crab pulsar parameters (magnetic moment $\mu \sim 10^{30.5}$ cgs, $\Omega \approx 200 \text{ s}^{-1}$, $\Phi \approx 4 \times 10^{16}$ V) and equatorial plasma properties inferred from our model of the wisp and ring dynamics ($Z = 1$ or 2, $m_i = Am_p$ with $A = 1$ or 4 and $2\kappa_\pm \sim 10^4$),

$$\sigma_{L0} \approx (1.3 - 1.7) \times 10^6 \gg 1. \quad (9)$$

Our model for the wisps' dynamics suggests $\gamma_{ion} \sim 0.1Ze\Phi/m_i c^2 \approx \sigma_{L0} \gg \sigma_{L0}^{1/3}$. Since laminar acceleration of the whole relativistic wind does not explain the inferred $\gamma_{ion} \approx \gamma_{wind} \sim 10^6$ or $\sigma_{wind}(r_s) \sim 10^{-2.5}$ in the equatorial flow (the only latitudes where we have substantial quantitative estimates for γ and σ in the wind), some additional physics must be at work to accelerate and demagnetize the wind in the equatorial sector.

The fact that the wisps (and the X-ray torus) lie in an angular sector near the pulsar's rotational equator and that these regions appear to accumulate the majority of the instantaneous rotational energy loss offers an important clue to the additional acceleration physics, a clue replicated in an increasing number of other young PWNs. That clue suggests that the equatorial region of this relativistic outflow has special properties not shared with the higher latitude regions, perhaps arising from the electric (return) current flowing in a crinkled sheet structure in an equatorial angular sector. Substantial theoretical evidence has accumulated to suggest that the $\sigma \gg 1$ regions of pulsar winds have structure close to that of a split monopole for r larger than a few times R_L . This result is quite certain for the aligned rotator, both from the asymptotic analysis (Michel 1974) and from the self-consistent numerical solution recently obtained by Contopoulos, Kazanas and Fendt (1999). While there is no similar demonstration that the asymptotic structure of the force-free oblique rotator's wind *must* be close to that of the oblique split monopole, whose field structure was recently obtained by Bogovalov (1999), we regard Bogovalov's model to be an excellent representation of the likely structure of the electromagnetic fields in the wind of an oblique rotator outside the light cylinder and will assume those fields in this discussion of wind acceleration.

In the equatorial sector $-i < \lambda < i$, with i the inclination angle between the magnetic moment and angular velocity vectors, the electromagnetic fields have the form

$$B_r = \frac{M}{r^2} f \left[\frac{r}{\beta R_L} - (\phi - \Omega t) \right],$$

$$B_\phi = -\frac{M \sin \theta}{r R_L} f \left[\frac{r}{\beta R_L} - (\phi - \Omega t) \right],$$

$$E_\theta = B_\phi, \quad B_\theta = E_r = E_\phi = 0. \quad (10)$$

tion dynamics is well described by force-free theory in a much more limited region than they assumed.

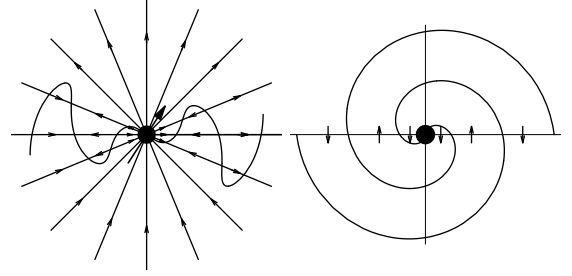


FIG. 4.— Frozen-in current sheet structure of the oblique split monopole in the inner wind. *Left*: Meridional cross-section of the poloidal field structure, showing the crinkled current sheet. The thick arrow indicates the instantaneous direction of the magnetic axis. Rotation is around the vertical axis. *Right*: Intersection of the current sheet with the equatorial plane. The toroidal magnetic field forms stripes with opposite directions between each current layer, as indicated by the arrows between the current sheets.

Here r, θ, ϕ are the spherical radius, colatitude (measured from a z -axis with positive z along the neutron star's angular velocity vector), and rotational azimuth, respectively, measured from an arbitrary x -axis with ϕ increasing in the direction of rotation. Furthermore, $f = \pm 1$ is a step function of pattern phase $(r/\beta R_L) + \phi - \Omega t$, where $c\beta$ is the radial outflow velocity. The fields reverse in sign every wavelength [at $r = (n+1)\pi\beta R_L/2$], while the magnitudes of the fields remain the same as those of the aligned split monopole. The effective monopole moment is $M = k\mu/R_L$, with k a constant on the order of unity; $k = 1.36$ in the Contopoulos et al. (1999) solution for the aligned rotator. A crinkled current sheet separates the regions of oppositely directed field, shown in Figure 4 (following Bogovalov 1999). As is the case with the Deutsch (1955) fields of the vacuum rotator, these fields form a spirally wound pattern that corotates with the star. Outside the equatorial sector, $f = \text{constant}$. For $i < \pi/2$, as is thought to be the case for the Crab pulsar (Yadigaroglu & Romani 1995), $f = 1$ for $0 \leq (\pi/2) - i$ and $f = -1$ for $(\pi/2) + i \leq \theta \leq \pi$.

In the global, ideal model of the current flow, the ions reside in the crinkled current sheet, which is frozen into the flow. Therefore, they participate in the same acceleration to which the plasma outside the current sheet is exposed. In the global wind models the current sheet has infinitesimal thickness. However, in reality the current flows in a crinkled layer of finite thickness and may be subject to dissipative processes that can lead to the release of magnetic energy in the equatorial sector in the many decades in radius between $r = R_{ff} < 10^2 R_L$ and $r = r_s = 10^9 R_L$. The dissipation of magnetic energy can lead to acceleration (and possibly heating) of the plasma (including the ions) to higher 4-velocities than is possible in the ideal flows so far studied. Whether such dissipation is inductive destruction of the current sheet, modeled as a sheet pinch (Coroniti 1990; Michel 1994; Lyubarsky & Kirk 2001, Kirk & Skjærassen 2003), or has something to do with the dissipation of relativistically strong electromagnetic waves (Melatos 1998), perhaps generated by instability of the current sheet and accelerating the ions through ponderomotive wave pressure (Arons 2003, 2004), remains an open question.

6. CONCLUSIONS

We have studied the internal structure and time variability of a collisionless shock in an electron-positron pair plasma with an energetically significant admixture of ions. Upon crossing the shock the ion component undergoes relativistic cyclotron instability that renders the shock structure very dy-

namic. The first loop of the $\mathbf{E} \times \mathbf{B}$ ion orbit achieves a limit-cycle behavior and acts as a quasi-periodic wave emitter with a period of half a local Larmor time of the ions. This time-dependence led us to apply our results to the collisionless termination shock in the inner Crab Nebula where we identify the wisps with turning points in the drift orbit of the ions. The limit cycle of the instability produces large amplitude magnetosonic waves on a time-scale of several months that proceed to move downstream from the shock. This time-scale is intrinsic to the model and associates the appearance of the wisps to the mechanism of variability within the shock structure. This is in contrast to other models that generally do not explain the origin of the wisp perturbations, only their subsequent evolution. Our model naturally makes the region between wisp 1 and wisp 2 in the optical (or the inner *Chandra* X-ray ring and the torus) behave like a near zone of a radiating antenna and prescribes the pattern of brightness fluctuations to wisps 1 and 2 and the moving wisps. This pattern has both a stationary component oscillating in brightness (inner *Chandra* ring and the torus region) and moving wisps that cross the region. That is why the snapshots of the inner nebula taken with insufficient temporal sampling register motion yet on average always see two major wisps that do not seem to leave.

The morphological agreement between the behavior of the wisp region in the Crab and the results of our simulations is an important argument in favor of the presence of ions in the pulsar outflows, which are often presumed to consist only of electron-positron pairs. Such ions are a natural candidate for the return current flow of the pulsar that starts at the auroral boundary of the polar cap and is then mapped into the equatorial current sheet. In order to get a fit to the nebular dynamics we require an ion injection rate of $10^{34.5} \text{ s}^{-1}$. The associated current is of the same order of magnitude as the Goldreich-Julian current of the Crab pulsar. Thus, by studying the interaction of the pulsar wind with the nebula we are able for the first time to get a window on the enigmatic electrodynamics of pulsars. Electrostatically, ions are the preferred return

current carrier for pulsars with $\Omega \cdot \boldsymbol{\mu} > 0$, which is thought to be the geometry applicable to the Crab pulsar (Yadigaroglu & Romani 1995). This means that for a rotator with antialigned rotation and magnetic axes, the equatorial current would be carried by electrons, and their effect on the nebula might be different from the Crab case.

The model of the time variability of collisionless shocks presented here is fairly general and can be applied to other PWNs, as well as other astrophysical sources where collisionless shocks arise. For the pulsar B1509-58 and the associated nebula Gaensler et al. (2002) estimate a variability period of on the order of 3-5 yr. For Vela the spacing of semicircular X-ray arcs implies a period of variability similar to the Crab, yet there are no similar wisps in that remnant. This could be explained if Vela rings are not features in the equatorial flow, but rather in the polar direction (similar to the Crab halo (Hester et al., 1995)). The differences might also be a consequence of the later evolutionary state of the Vela PWN, where the environment has a chance to influence the termination of the pulsar's wind (Chevalier 1998, 2004). This underscores how much we are dependent on a reliable deconvolution of the geometry and the evolutionary history in all attempts to characterize the physics of non-thermal nebula energization by central compact objects. For sources other than the PWNs, collisionless shocks are common in relativistic AGN jets and thought to occur in gamma-ray bursts. Both settings are known to be quite variable, and whether ion-cyclotron instability can operate in these shocks remains to be studied.

We acknowledge assistance from NASA grants NAG5-12031 and HST-AR-09548.01-A. J.A. thanks the Miller Institute for Basic Research in Science and the taxpayers of California for their support. A.S. acknowledges support provided by NASA through Chandra Fellowship grant PF2-30025 awarded by the Chandra X-Ray Center, which is operated by the Smithsonian Astrophysical Observatory for NASA under contract NAS8-39073.

APPENDIX

APPENDIX: MODEL DERIVATION AND SIMULATION DETAILS

Evolution equations for a time-dependent shock in the pair-ion system can be obtained from the divergence of the full energy-momentum tensor $T^{\alpha\beta} = n_i m_i c^2 u_i^\alpha u_i^\beta + w u^\alpha u^\beta + P^{\alpha\beta} + T_{\text{EM}}^{\alpha\beta}$. Here $n_i m_i c^2$ is the rest energy density for ions, $u = (\gamma, \gamma\boldsymbol{\beta})$ and $u_i = (\gamma_i, \gamma_i\boldsymbol{\beta}_i)$ are 4-velocities of the pair and ion components, respectively, w is the enthalpy of the pairs, $P^{\alpha\beta}$ is the pressure tensor, and $T_{\text{EM}}^{\alpha\beta}$ is the electromagnetic stress-energy tensor. We assume that ion fluid is cold compared to pairs; thus, only pair pressure enters into $P^{\alpha\beta}$. Beyond the shock the dynamics of the pairs is initially constrained to be in the plane orthogonal to the toroidal magnetic field B_ϕ ; therefore, we should allow for potentially anisotropic pressure: $P^{tt} = -P_\perp$, $P^{rr} = P^{\theta\theta} = P_\perp$, $P^{\phi\phi} = P_\parallel$. Allowing only for spatial variation in r for all quantities, the continuity equations together with the momentum and energy conservation laws and induction equation in spherical coordinates around the equatorial plane are then:

$$\frac{\partial}{\partial ct}(n_\pm \gamma) + \frac{1}{r^2} \frac{\partial}{\partial r}(r^2 n_\pm \gamma \beta_r) = 0, \quad (\text{A1})$$

$$\frac{\partial}{\partial ct}(n_i \gamma) + \frac{1}{r^2} \frac{\partial}{\partial r}(r^2 n_i \gamma \beta_{ir}) = 0, \quad (\text{A2})$$

$$\begin{aligned} \frac{\partial}{\partial ct}(n_i \gamma_i m_i c^2 u_{ir} + w \gamma u_r + \frac{1}{4\pi} E_\theta B_\phi) + \frac{1}{r^2} \frac{\partial}{\partial r}[r^2(n_i m_i c^2 (u_{ir})^2 + w (u_r)^2 - \frac{1}{8\pi} (E_r^2 \\ - E_\theta^2 - B_\phi^2))] + \frac{1}{r^2} \frac{\partial}{\partial r} P_\perp + \frac{P_\perp - P_\parallel}{r} - \frac{1}{r}(n_i m_i (u_{i\theta})^2 + w (u_\theta)^2) - \frac{E_r^2}{4\pi r} = 0, \end{aligned} \quad (\text{A3})$$

$$\begin{aligned} \frac{\partial}{\partial ct}(n_i \gamma_i m_i c^2 u_{i\theta} + w \gamma u_\theta - \frac{1}{4\pi} E_r B_\phi) + \frac{1}{r^2} \frac{\partial}{\partial r}[r^2(n_i m_i c^2 u_{ir} u_{i\theta} + w u_r u_\theta - \frac{1}{4\pi} E_r E_\theta) \\ + \frac{1}{r}[n_i m_i c^2 u_{ir} u_{i\theta} + w u_r u_\theta - \frac{1}{4\pi} E_r E_\theta] = 0, \end{aligned} \quad (\text{A4})$$

$$\frac{\partial}{\partial ct} [n_i m_i c^2 \gamma_i^2 + w \gamma^2 - P_\perp + \frac{1}{8\pi} (E^2 + B^2)] + \frac{1}{r^2} \frac{\partial}{\partial r} [r^2 (n_i m_i c^2 \gamma_i u_{ir} + w \gamma u_r + \frac{1}{4\pi} E_\theta B_\phi)] = 0, \quad (\text{A5})$$

$$\frac{\partial}{\partial ct} B_\phi + \frac{1}{r^2} \frac{\partial}{\partial r} (r^2 B_\phi \beta_r) - \frac{B_\phi \beta_r}{r} = 0. \quad (\text{A6})$$

In (A6) we used the MHD condition $E + \beta \times B = 0$. It can be shown that for variations on the ion cyclotron time-scale and moderate harmonics thereof, departures from ideal MHD in the pairs are negligible.

We proceed to normalize all dimensional quantities in these equations in terms of the upstream ion gyration radius and cyclotron time as in §2. Using the normalized quantities and the generalized adiabatic index for anisotropic pressure as defined in §2, the enthalpy can be written as $w = \rho(1 + \Gamma/(\Gamma - 1)P_\perp/\rho) \equiv \rho h$, where ρ is the rest energy density of the pairs, and h is the specific enthalpy. Using the equations of motion for the ions,

$$\frac{du_{ir}}{dct} - \frac{1}{r} \frac{(u_{i\theta})^2}{\gamma_i} = \frac{Ze}{m_i} [E + \frac{u_i}{\gamma_i} \times B]_r, \quad (\text{A7})$$

$$\frac{du_{i\theta}}{dct} + \frac{1}{r} \frac{u_{i\theta} u_{ir}}{\gamma_i} = \frac{Ze}{m_i} [E + \frac{u_i}{\gamma_i} \times B]_\theta, \quad (\text{A8})$$

we can rewrite the normalized pair equations (A1-A6) as follows:

$$\frac{\partial}{\partial t} (\rho \gamma) + \frac{1}{r^2} \frac{\partial}{\partial r} (r^2 \rho \gamma \beta_r) = 0, \quad (\text{A9})$$

$$\begin{aligned} \frac{\partial}{\partial t} (\rho h \gamma^2 \beta_r + \sigma_\pm \beta_r B_\phi^2) + \frac{1}{r^2} \frac{\partial}{\partial r} [r^2 (\rho h \gamma^2 \beta_r^2 + \frac{1}{2} \sigma_\pm (1 - \beta_\theta^2 + \beta_r^2) B_\phi^2)] \\ + \frac{1}{r^2} \frac{\partial}{\partial r} P_\perp + \frac{P_\perp - P_\parallel}{r} - \frac{1}{r} \rho h \gamma^2 \beta_\theta^2 - \sigma_\pm \frac{1}{r} \beta_\theta^2 B_\phi^2 + \epsilon N_i (\beta_{i\theta} - \beta_\theta) B_\phi = 0, \end{aligned} \quad (\text{A10})$$

$$\begin{aligned} \frac{\partial}{\partial t} (\rho h \gamma^2 \beta_\theta + \sigma_\pm \beta_\theta B_\phi^2) + \frac{1}{r^2} \frac{\partial}{\partial r} [r^2 (\rho h \gamma^2 \beta_r \beta_\theta + \sigma_\pm \beta_r \beta_\theta B_\phi^2)] \\ + \frac{1}{r} [\rho h \gamma^2 \beta_r \beta_\theta + \sigma_\pm \beta_r \beta_\theta B_\phi^2] + \epsilon N_i (\beta_r - \beta_{ir}) B_\phi = 0, \end{aligned} \quad (\text{A11})$$

$$\begin{aligned} \frac{\partial}{\partial t} [\rho h \gamma^2 - P_\perp + \frac{1}{2} \sigma_\pm (1 + \beta_r^2 + \beta_\theta^2) B_\phi^2] \\ + \frac{1}{r^2} \frac{\partial}{\partial r} [r^2 (\rho h \gamma^2 \beta_r + \sigma_\pm \beta_r B_\phi^2)] + \epsilon N_i (\beta_{i\theta} \beta_r - \beta_{ir} \beta_\theta) B_\phi = 0, \end{aligned} \quad (\text{A12})$$

$$\frac{\partial}{\partial t} B_\phi + \frac{1}{r^2} \frac{\partial}{\partial r} (r^2 B_\phi \beta_r) - \frac{B_\phi \beta_r}{r} = 0. \quad (\text{A13})$$

where energy fractions σ_\pm , σ_i and ϵ are defined in (6). For flows with low magnetization such that $\sigma_\pm \rightarrow 0$, $\sigma_i \rightarrow 0$, but ϵ finite, these equations reduce to the system (1-4). The Poisson equation and Ampere's law can be written in terms of normalized quantities as

$$\rho_\pm + \rho_i = \sigma_i \nabla \cdot E, \quad (\text{A14})$$

$$j_\pm + j_i = \sigma_i (\nabla \times B - \frac{\partial}{\partial t} E), \quad (\text{A15})$$

where the charge densities of the pair fluid (ρ_\pm) and the ions (ρ_i) are normalized in terms of the upstream ion density N_{i1} , and similarly for the currents j_\pm , j_i . When σ_i is small, field gradients are on scales commensurate with r_{i1} in all directions, and time evolution is on scales ω_{ci1}^{-1} , the expressions on the right-hand side of (A14, A15) can be neglected and the flow is charge and current quasi-neutral.²

We have developed a code that solves the full equations (A9-A13); however, for the region inside of the X-ray torus in the Crab Nebula, which is the region of interest for the wisp dynamics, the inclusion of the magnetization does not change our results. It is important to include these terms to study the evolution of the flow in the outer nebula where the magnetic field is compressed to equipartition, so in the following we describe the structure of the full simulation.

We discretize eqs. (1-4) on an equidistant grid in radius ranging from 0.1 to $10r_{Li1}$ with 1000 cells. Our simulation domain contains both the regions of supersonic flow upstream of the shock and the subsonic downstream region, while the position of the shock is determined dynamically. To advance the pair equations, we use the Lax-Friedrichs central-difference forward-in-time scheme. Despite its simplicity, it handles well both the upstream and the downstream regions, including wave propagation and scattering off the shock. To maintain numerical stability of a centered scheme, the method introduces inherent diffusivity, which spreads the reverse shock over 10 cells. This is not a concern since the shock is still very well localized on the grid, and the wave amplitude diffusion is less than 10% over the simulation domain. At every timestep we advance the following conservative variables: $D = \rho \gamma$, $F = \rho h \gamma^2 \beta_r + \sigma_\pm \beta_r B_\phi^2$, $G = \rho h \gamma^2 \beta_\theta + \sigma_\pm \beta_\theta B_\phi^2$, and $\tau = \rho h \gamma^2 - P_\perp + \frac{1}{2} \sigma_\pm (1 + \beta_r^2 + \beta_\theta^2) B_\phi^2$. These variables need to be converted to the primitive variables ρ , P_\perp , $\beta_{r,\theta}$, and B_ϕ . We use a numerical root-finding routine to solve for pressure P_\perp from $P_\perp = (\Gamma - 1)\epsilon_*$, where the energy density ϵ_* is given by

$$\epsilon_* = [\tau + D(1 - \gamma_*) + P_\perp(1 - \gamma_*^2) - \sigma_\pm B_\phi^2(2 - \frac{1}{\gamma_*})] \frac{1}{\gamma_*}. \quad (\text{A16})$$

² We are indebted to Z.-Y. Li, who first pointed out this possible simplification to us.

At every iteration of the root finding the Lorentz factor γ_* is expressed as a function of τ , F , G , P_\perp , and B_ϕ through

$$\gamma_*^2 = \frac{(\tau + P_\perp + \frac{1}{2}\sigma_\pm B_\phi^2/\gamma_*^2)^2}{(\tau + P_\perp + \frac{1}{2}\sigma_\pm B_\phi^2/\gamma_*^2)^2 - (F^2 + G^2)}, \quad (\text{A17})$$

which can be reduced to a cubic in γ_*^2 . Having found P_\perp and γ , pair flow velocities are obtained from

$$\beta_r = \frac{F}{\tau + P_\perp + \frac{1}{2}\sigma_\pm \frac{B_\phi^2}{\gamma^2}}, \quad (\text{A18})$$

$$\beta_\theta = \frac{G}{\tau + P_\perp + \frac{1}{2}\sigma_\pm \frac{B_\phi^2}{\gamma^2}}. \quad (\text{A19})$$

The initial state for the calculation is the steady state strong MHD shock. We construct this state by first computing the jump conditions between the upstream (subscript 1) and downstream (subscript 2) side of the shock from:

$$\rho_1 \gamma_1 \beta_{r1} = \rho_2 \gamma_2 \beta_{r2}, \quad (\text{A20})$$

$$\rho_1 \gamma_1^2 \beta_{r1}^2 + \frac{1}{2}\sigma_\pm(1 + \beta_{r1}^2)B_{\phi 1}^2 = \rho_2 h_2 \gamma_2^2 \beta_{r2}^2 + \frac{1}{2}\sigma_\pm(1 + \beta_{r2}^2)B_{\phi 2}^2 + P_{\perp 2}, \quad (\text{A21})$$

$$\rho_1 \gamma_1^2 \beta_{r1} + \sigma_\pm \beta_{r1} B_{\phi 1}^2 = \rho_2 h_2 \gamma_2^2 \beta_{r2} + \sigma_\pm \beta_{r2} B_{\phi 2}^2, \quad (\text{A22})$$

$$B_{\phi 1} \beta_{r1} = B_{\phi 2} \beta_{r2}, \quad (\text{A23})$$

where the normalized quantities on the upstream side are given by $\gamma_1 = 10^6$, $B_{\phi 1} = 1$, $\rho_1 = \frac{1}{\gamma_1}$, the flow is cold, $P_{\perp 1} = 0$, and is assumed to have no θ -component of velocity. Although there exist analytical approximations to the jump conditions for various limiting values of σ_\pm (Kennel and Coroniti 1984a), we solve the general case numerically. Having found the jump conditions, we select the radius of the shock r_s (typically, $r_s = 1r_{Li1}$) and solve for the steady state flow from conservation laws (A9-A12) with the time derivatives omitted.

The flow solution can be expressed in terms of constants $c_1 = r^2 \gamma \rho \beta_r$ from the equation of continuity, $c_2 = r^2 \rho h \gamma^2 \beta_r^2 + r^2 \sigma_\pm \beta_r B_\phi^2$ from the energy equation and $c_3 = r B_\phi \beta_r$ from the induction equation. These constants can be evaluated at the shock and then used together with the equation of state to express P_\perp , ρ , and B_ϕ as a function of β_r . When substituted into the momentum equation

$$\frac{1}{r^2} \frac{\partial}{\partial r} [r^2 (\rho h \gamma^2 \beta_r^2 + \frac{1}{2}\sigma_\pm(1 - \beta_\theta^2 + \beta_r^2)B_\phi^2)] + \frac{1}{r^2} \frac{\partial}{\partial r} P_\perp + \frac{P_\perp - P_\parallel}{r} = 0, \quad (\text{A24})$$

we get a differential equation for β_r , which is integrated numerically inward and outward from the shock to obtain the flow solution.

The dynamical evolution equations (A9-A12) are driven by the currents induced in the pairs by the motion of the ions. To compute the ion quantities N_i and $\beta_{i,r,\theta}$, we use the 1.5-dimensional particle-in-cell method. Ions are represented as macroparticles whose velocities are calculated by advancing eqs. (A7-A8). The fields are extrapolated from the grid to the positions of the particles, and after advance the particle densities and currents are deposited at gridpoints. In both of these operations we utilize volume weighting to properly account for the diverging spherical geometry.

The simulation domain is augmented by a buffer zone of width equal to 1 r_{Li1} where the field is kept constant. This zone is needed to accurately represent the contribution of ions that would normally leave the domain and then reenter the outer edge of the grid as part of their $\mathbf{E} \times \mathbf{B}$ trajectory. The outer boundary conditions are designed to mimic the rest of the nebula that is not simulated and to reduce the unwanted reflections. Two methods are used for this. For simulations with $f \equiv r_{Li1}/r_s \ll 1$, or essentially planar geometry, the reflections off the right edge in subsonic outflow can be minimized by applying the method of characteristic decomposition (Thompson 1987). The method works by explicitly setting the left-going characteristics to zero at the boundary. For simulations with significant spherical geometry effects ($f \sim 1$) less complicated boundary conditions of variable extrapolation produce acceptable results.

REFERENCES

- Alsop, D. & Arons, J. 1988, *Phys. Fl.*, 31, 839
Arons, J. 2003, *ApJ*, 589, 871
Arons, J. 2004, *Adv. Space Res.*, in press
Bandiera, R., Amato, E., & Woltjer, L. 1998, *Mem. Soc. Astron. It.*, 69, 901
Bednarz, J., & Ostrowski, M. 1996, *MNRAS*, 283, 447
Begelman, M.C., & Li, Z.-Y. 1994, *ApJ*, 426, 269
Begelman, M. C. 1999, *ApJ*, 512, 755
Beskin, V.S., Kuznetsova, I.V., & Rafikov, R.R. 1998, *MNRAS*, 299, 341
Bietenholz, M. F., Frail, D. A., and Hester, J.J. 2001, *ApJ*, 560, 254
Birdsall, C. K., & Langdon A. B. 1991, *Plasma Physics via Computer Simulation* (New York: Adam Hilger)
Blandford, R. 2002, in 'Lighthouses of the Universe', M. Gilfanov, R. Sunyaev et al. (Munich:ESO), 381
Bogovalov, S. 1999, *A&A*, 349, 1017
Chedia, O., Lominadze, J., Machabeli, G., Mchedlishvili, G., Shapakidze, D. 1997, *ApJ*, 479, 313
Chevalier, R. A. 1998, *Mem. Soc. Astron. It.*, 69, 977
Chevalier, R. A. 2004, *Adv. Space Res.*, in press, astro-ph/0301370
Contopoulos, I., Kazanas, D., & Fendt, C. 1999, *ApJ*, 511, 351
Contopoulos, I., Kazanas, D. 2002, *ApJ*, 566, 336
Coroniti, F. V. 1990, *ApJ*, 349, 538
de Jager, O. C., Harding, A. K. 1992, *ApJ*, 396, 161
Deutsch A 1955, *Annales d'Astrophysique*, 18, 1
Gaensler, B. M., Arons, J., Kaspi, V. M., Pivovarov, M. J., Kawai, N., Tamura, K. 2002, *ApJ*, 569, 878
Gallant, Y. A., & Arons, J. 1994, *ApJ*, 435, 230
Gallant, Y. A., Hoshino, M., Langdon, A. B., Arons, J., Max, C. E. 1992, *ApJ*, 391, 73
Gallant, Y. A. 2002, *Lecture Notes in Physics*, 589, 24

- Goldreich, P., and Julian, W. 1970, *ApJ*, 160, 971
- Harding, A. K., & Muslimov, A. G. 1998, *ApJ*, 500, 862
- Hester, J. J., Scowen, P. A., Sankrit, R., Burrows, C. J., Gallagher, J. S., III, Holtzman, J. A., Watson, A., Trauger, J. T., Ballester, G. E., Casertano, S., et al. 1995, *ApJ*, 448, 240
- Hester, J. J. 1998, *Mem. Soc. Astron. It.*, 69, 883
- Hester, J. J. 1998, *Rev. Mex. Ast. Ast.*, 7, 90
- Hester, J. J., Mori, K., Burrows, D., Gallagher, J. S., Graham, J. R., Halverson, M., Kader, A., Michel, F. C., Scowen, P. 2002, *ApJ*, 577, L49
- Hibschmann, J. A., & Arons, J. 2001, *ApJ*, 560, 871
- Hoshino, M., & Arons, J. 1991, *Phys. Fluids B*, 3, 818
- Hoshino, M., Arons, J., Gallant, Y. A., & Langdon, A. B. 1992, *ApJ*, 390, 454
- Kennel, C. F., & Coroniti, F. V. 1984a, *ApJ*, 283, 694
- Kennel, C. F., & Coroniti, F. V. 1984b, *ApJ*, 283, 710
- Kirk, J.G., & Skjæraasen, O. 2003, *in press* (astro-ph/0303194)
- Komissarov, S., & Lyubarsky, Y. 2003, *MNRAS*, 344, L93
- Krolik, J. H. 1999, "Active Galactic Nuclei" (Princeton: Princeton University Press)
- Lampland, C. O. 1921, *Pub. A. S. P.*, 33, 79
- Lyubarsky, Y. & Kirk, J. G. 2001, *ApJ*, 547, 437
- Langdon, A.B., Arons, J. & Max, C. E. 1988, *Phys. Rev. Lett.*, 61, 779
- Melatos, A. 1998, *Mem. Soc. Ast. It.*, 69, 1009
- Melatos, A., & Melrose, D. B. 1996, *MNRAS*, 279, 1168
- Michel, F. C. 1969, *ApJ*, 158, 727
- Michel, F. C. 1974, *ApJ*, 187, 585
- Michel, F. C. 1994, *ApJ*, 431, 397
- Mori, K., Hester, J. J., Burrows, D. N., Pavlov, G. G., Tsunemi, H. 2002, *PASP*, 271, 157
- Muslimov, A. G., & Harding, A. K. 2003, *ApJ*, 588, 430
- Rees, M. J., & Gunn, J. E. 1974, *MNRAS*, 167, 1
- Scargle, J. D. 1969, *ApJ*, 156, 401
- Scargle, J. D., & Harlan, E. A. 1970, *ApJ*, 159, L143
- Scargle, J. D., & Pacini F. 1971, *Nature*, 232, 144
- Tanvir, N. R., Thomson, R. C., Tsikarishvili, E. G. 1997, *New Astr.*, 1, 311
- Thompson, K. W. 1987, *J. Comp. Phys.*, 68, 1
- van den Bergh, S., & Pritchett, C. J. 1989, *ApJ*, 338, L69
- Weisskopf, M. C., Hester, J. J., Tennant, A. *F.et al.* 2000, *ApJ*, 536, 81
- Yadigaroglu, I.-A., & Romani, R. W. 1995, *ApJ*, 449, 211
- Yang, T.-Y. B., Gallant, Yves, Arons, Jonathan & Langdon, A. B. 1993, *Phys. Fluids B*, 5, 3369
- Yang, T.-Y. B., Arons, Jonathan & Langdon, A. B. 1994, *Phys. Plasmas*, 1, 3059